

## RESEARCH ARTICLE

# Design of an In-Pipe Robot Coupled With Multiple Cams

QIZHI XIE<sup>1</sup>, SONG CUI<sup>2</sup>, PEILIN CHENG<sup>3</sup>, AND QIANG LIU<sup>2,4</sup><sup>1</sup>School of Mechanical and Electrical Engineering, Xuzhou University of Technology, Xuzhou 221018, China<sup>2</sup>School of Mechatronic Engineering, China University of Mining and Technology, Xuzhou 221116, China<sup>3</sup>School of Mechanical Engineering, Zhejiang Sci-Tech University, Hangzhou 310018, China<sup>4</sup>School of Physics and New Energy, Xuzhou University of Technology, Xuzhou 221018, China

Corresponding author: Qizhi Xie (qzxiexie@163.com)

This work was supported in part by the Jiangsu Province Industry University Research Cooperation Project BY2022760, and in part by the Natural Science Foundation of the Jiangsu Higher Education Institutions of China under Grant 19KJB460026.

**ABSTRACT** The inchworm in-pipe robot has the advantages of stable support, low walking resistance, and high flexibility. However, the gait motion of in-pipe robots relies on the precise coordination of three motors, which greatly increases the complexity of control. To solve this problem, an inchworm in-pipe robot based on a multi-cam combination is proposed. The robot needs only one motor to achieve active support and bidirectional crawling for the pipe wall, mainly used for detecting straight pipelines, such as the main drainage pipeline. In order to obtain the periodic motion law and characteristics of the inchworm in-pipe robot, structure design, constraint analysis, and dynamic simulation were carried out on the robot. Finally, the principle prototype was tested in the transparent pipe, the test results indicate that the robot can achieve bidirectional creep under a single motor drive, which can simplify the control of gait motion for inchworm in-pipe robots. The average displacement errors for horizontal walking and vertical walking are 2.0% and 11.3%, respectively, due to factors such as gravity. Therefore, the robot can achieve a more accurate step distance in the horizontal pipe.


**INDEX TERMS** In-pipe robot, inchworm, single-drive, cam-based, constraint analysis.

## I. INTRODUCTION

Pipelines are vital infrastructures in oil and gas, water, and sewage transfer, in order to ensure the safety of the pipeline, the use of in-pipe robots for labor intensive and hazardous operations, has increased in recent years [1], [2].

The in-pipe robot can be classified into several classical forms according to the existing moving modes and contact forms with the pipe wall. These include wheel type [3], tracked type [4], inchworm type [5], magnetic type [6], walking type [7], screw type [8], and swimming type [9], [10]. Wheeled robots are usually driven by motors, and their driving force mainly depends on the positive pressure of the driving wheel on the pipe wall when the motor power and friction coefficient are constant. Thung-Od et al. [11] presented the design and prototype of an inspection robot with permanent magnets and omnidirectional wheels, which

can perform both horizontal and vertical locomotion in ferromagnetic pipelines. The train-like robot is mainly composed of three sealed modules and is driven by multiple motors. Miao et al. [12] proposed a multi-module in-pipe robot for the pipeline isolation plugging, which mainly includes a pressure head, a squeeze bowl, an actuator plate, and a plug. Sawabe et al. [13] proposed a control method for articulated wheeled mobile robots. This type of robot has many drivers and relatively complex control. Zhang et al. [14] designed a wall-press wheeled in-pipe robot with active pipe-diameter adaptability, which have three sets of wheels circularly located 120° apart from each other. The walking characteristics of wheeled in-pipe robots largely depend on the contact between the wheels and the pipe. Unfortunately, due to the driving wheels always firmly press the wall during the move, their forward resistance will increase with increasing support force when the wall is not flat, thus, the energy consumption increases. The motion of the magnetic in-pipe robot does not require the use of wheels, but requires the use

The associate editor coordinating the review of this manuscript and approving it for publication was Aysegül Ucar .

of external magnetic fields. For example, Munoz et al. [15] proposed a capsule in-pipe robot for drug transportation, which manipulates the robot using magnetic fields generated by multiple curved permanent magnets. The magnetic in-pipe robot is usually used for microenvironment operations and has a small load capacity.

Unlike wheeled in-pipe robots that walk in a straight line, helical in-pipe robots achieve spiral motion by tilting a set of wheels or controlling the magnetic field. Shiomi et al. [16] designed a slender flexible in-pipe robot that mimics the behavior of spirochete microorganisms and spirals through the pipeline. Nam et al. [17] proposed a magnetic helical robot (HR) that can helically navigate, release a drug to a target area. Li et al. [18] designed a screw drive in-pipe robot with an adaptive linkage mechanism based on the adaptive movement mechanism. Ren et al. [19], [20], [21], [22] proposed a series of spiral driven robots based on gear or belt pulley transmission, and analyzed the basic characteristics of the robots. Li et al. [23] proposed an oil and gas in-pipe robot with a helical drive, geometric calculation and mechanical analysis were carried out to help design the robot.

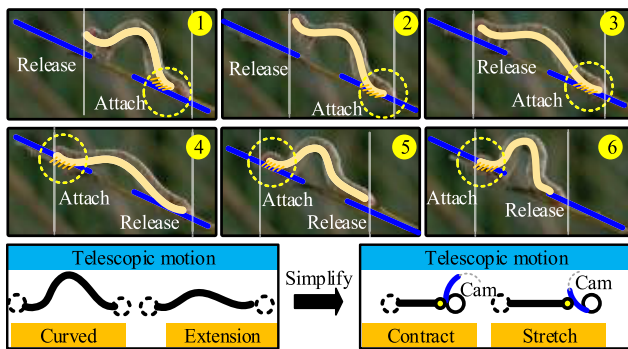


FIGURE 1. Gait principle of inchworm.

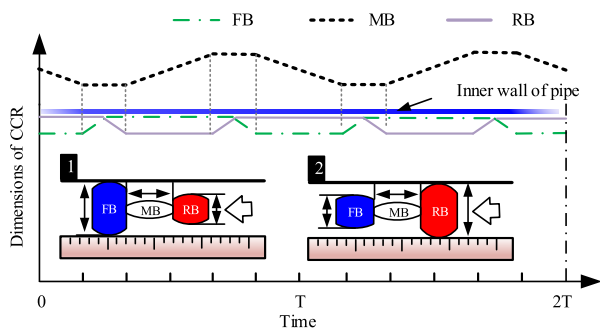


FIGURE 2. Bionic principle of inchworm.

Compared with the wheel type, the inchworm type has a large contact area with the pipe wall. Therefore, more and more scholars are studying the inchworm in-pipe robot. The design idea of the inchworm in-pipe robot is derived from the inchworm in Fig. 1. The robot adopts a gait walking mode and a split structure, and has the characteristics of good stability, low walking resistance, and strong flexibility.

The characteristics of gait motion in Fig. 2 are realized by alternating movements of the front body (FB), the middle body (MB) and the rear body (RB) of the robot in chronological order. For example, Fang et al. [24] proposed a worm-like in-pipe robot with a rigid and soft structure, which has flexible mobility in the shaped pipes. Ito et al. [25] proposed an earthworm in-pipe robot using pneumatic artificial muscles, which can install wires in complex pipelines. Liu and Dai et al. [26], [27] proposed an inchworm in-pipe robot based on the concept of a tensioned whole, which is a self-stressing spatial structure composed of discrete rigid pillars. Tang et al. [28] proposed an intelligent material-driven in-pipe robot that can be installed in pipelines less than one centimetre in diameter, and the dielectric elastomer actuator is used as the driving force. Liu et al. [29] proposed a vacuum-driven inclined hexagonal prism soft-rigid hybrid contraction actuator inspired by the Kresling origami pattern. However, the control system of the inchworm in-pipe robot is complex, it is usually driven by multiple motors, the number of power cables and the drag cable resistance is large, which limits the inspection distance of the robot.

The implementation methods for single-drive inchworm robots were designed to simplify robot control and reduce the number of drives. For instance, Qiao et al. [30] proposed a self-lock inchworm in-pipe robot, the support force is produced by wedges between the robot and inner pipe wall. However, the robot can only walk in one direction because the inclined direction of wedges has been determined beforehand, unless an additional driver is added to change the direction of the wedge, which increases the complexity of the mechanism and control. Zarrouk et al. [31] proposed an inchworm in-pipe robot driven by a single motor. The robot uses a spiral axis to arrange and coordinate cells and fixtures. This design makes the robot miniaturized and reduces the control complexity and cost. The robot can move forward, backward and vertically with low power consumption. However, the leg of this kind of robot does not have the ability of active contraction, and it always contacts with the pipe wall during the whole movement, so the end of the leg will have sliding friction, which accelerates the wear.

To solve the above problems, a multi-cam based in-pipe robot called CCR (Cam-Cam Robot) has been presented to overcome the above limitations. CCR can realize active support to the pipe wall and double-direction gait motion via only one motor. The multi-cam combination mechanism is the core mechanism of CCR, which can realize the intermittent walking of robot in horizontal and vertical pipeline. In addition, the structure design and constraint analysis of the robot were carried out, and mechanical properties and traction energy efficiency ratio were analyzed. Finally, the correctness and practicability of the design principle of the robot were verified by experiments.

## II. STRUCTURE DESIGN

According to the motion position, CCR robot can be divided into three modules: front body, middle body and rear body.

According to the function, it can be divided into two modules: the radial expansion module and the axial expansion module. The radial expansion module is used to support the pipe wall, and the axial expansion module is used to propel the robot along the pipe axis.

As shown in Fig. 3(a), the power from the motor is transmitted to the cam via spur and bevel gears. The cam can convert the rotary motion of the motor into linear motion of the push rod, so that radial expansion motion can be achieved by the cam mechanism. When the motor rotates continuously, the push rod can still stop, so the cam mechanism can achieve the intermittent motion. From Fig. 3(b), the axial expansion of the robot need to be driven, but there is only one driving motor, so it is necessary to design a transmission mechanism to transmit the power to the front and rear of the robot, which is realized by bevel gear and expansion drive shaft, so single input and multiple output can be realized in Fig. 3(c).

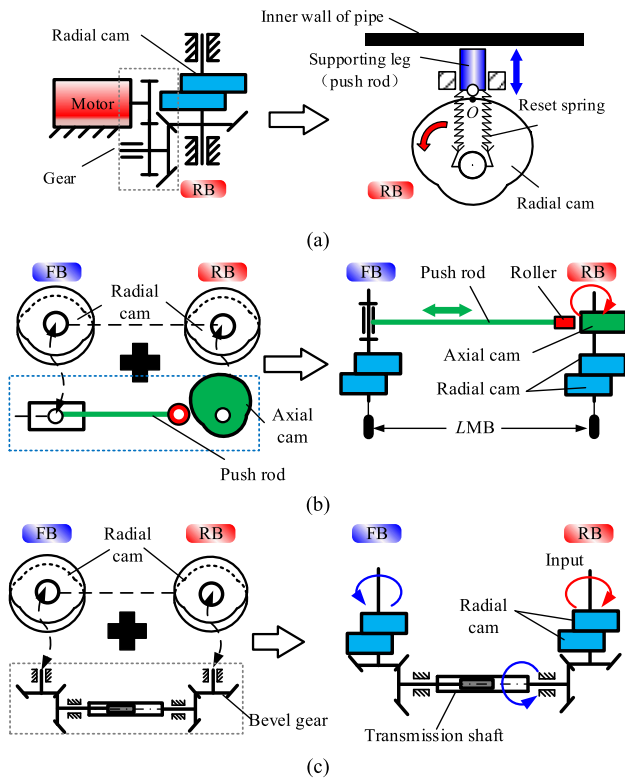


FIGURE 3. Mechanism principle and structure design of CCR. (a) motor drive. (b) telescoping motion. (c) mechanical transmission.

The three-dimensional structure of the robot is shown in Fig. 4. The FB or RB of the robot is supported by ball wheels and rubber pads on the pipe wall, which can also serve as a guide and provide sufficient support. The mobile pairs are realized by linear bearings, which can effectively avoid the self-locking of the mobile pairs and reduce the friction energy loss. In Fig. 5, the robot can walk in two-way peristalsis. The principle of two-way walking is that when the RB is stationary, the FB moves to the left, then the FB is stationary, and the RB moves to the left, so that the robot can continue to

walk to the left; otherwise, the robot continues to walk to the right. The robot proposed in this paper only needs to control the rotation direction of the motor to realize the forward and reverse walking.

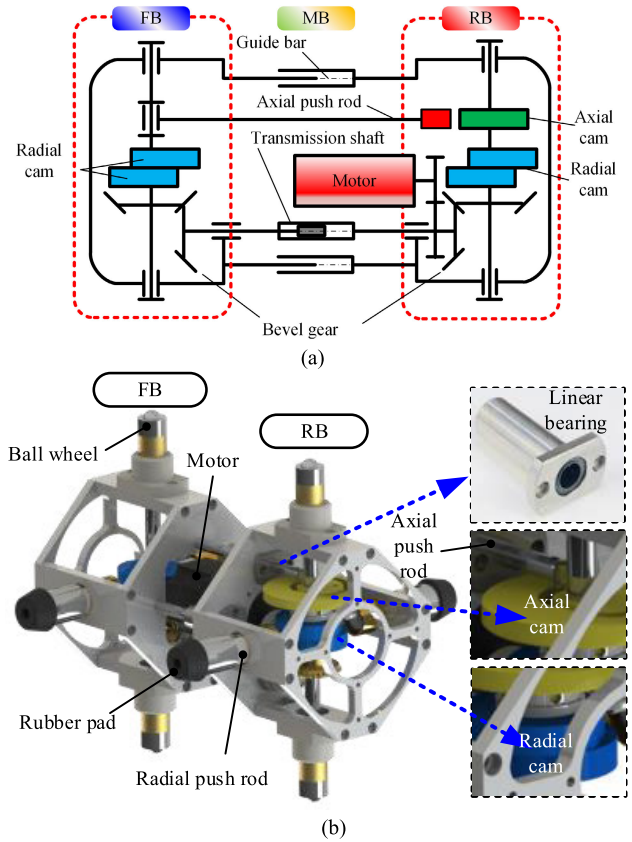


FIGURE 4. Mechanism principle and structure design. (a) 2D. (b) 3D.

### III. ANALYSIS OF MOTION LAW

The robot's telescoping motion is realized by cam mechanism, the motion law of the push rod (follower) is generally described as the relationship between the displacement of the push rod and the cam angle.

#### A. MOTION LAW

The motion law of the push rod usually has the polynomial motion law and the triangle function motion law, the cosine acceleration motion law, equation of radial push motion is as follows:

$$\begin{cases} s = \frac{h}{2} [1 - \cos \frac{\pi}{\delta_0} \delta] \\ \frac{ds}{d\delta} = \frac{\pi h}{2\delta_0} \sin(\frac{\pi}{\delta_0} \delta) \\ \frac{d^2s}{d\delta^2} = \frac{\pi^2 h}{2\delta_0^2} \cos(\frac{\pi}{\delta_0} \delta) \\ \frac{d^3s}{d\delta^3} = -\frac{\pi^3 h}{2\delta_0^3} \sin(\frac{\pi}{\delta_0} \delta) \end{cases} \quad (1)$$

where  $s$  is the displacement of the push rod;  $h$  is the stroke of the push rod,  $\delta$  is the cam angle,  $\delta_0$  is the cam angle for actuating travel (rise segment).

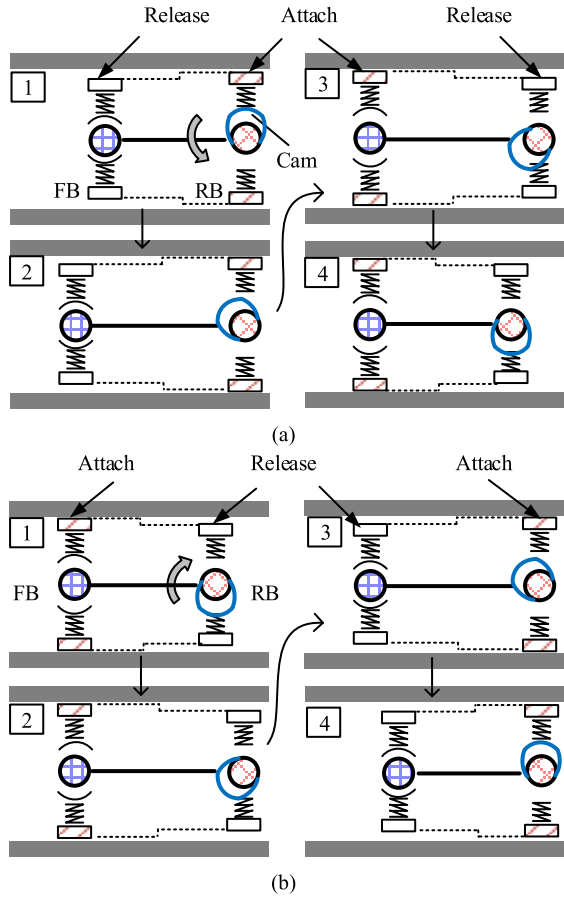


FIGURE 5. Two way motion principle. (a) Forward. (b) Reverse.

**B. CAM PROFILE**

According to the working requirements, after selecting the motion law of the push rod, the design of the cam profile should be carried out. The theoretical profile of the cam is generally carried out by the analytical method, which can obtain enough accuracy requirements. It is assumed that  $XOY$  is the absolute coordinate system, and the relative coordinate system is obtained by rotation or symmetrical transformation of the absolute coordinate system. It is assumed that the relative coordinate of the theoretical cam profile of each segment is calculated as follows:

$$\begin{cases} x = (r_0 + s) \sin \delta \\ y = (r_0 + s) \cos \delta \end{cases} \quad (2)$$

where  $r_0$  is the radius of the base circle, which is the minimum radius of the cam.

The analytic expression of cam working profile equation:

$$\begin{cases} x' = x \mp r_r \frac{(-\dot{y})}{\sqrt{\dot{x}^2 + \dot{y}^2}} \\ y' = y \mp r_r \frac{\dot{x}}{\sqrt{\dot{x}^2 + \dot{y}^2}} \end{cases} \quad (3)$$

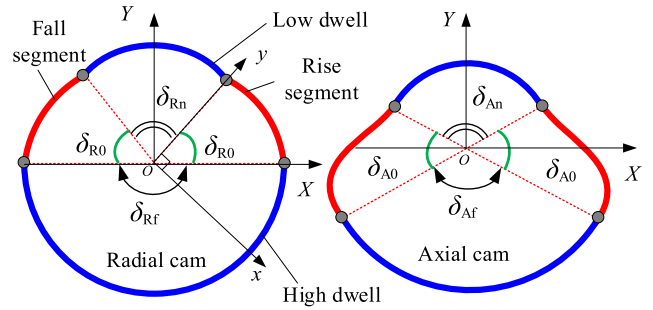


FIGURE 6. Absolute coordinate system  $XOY$  of four segment cam.

As shown in Fig. 6, according to the geometric relationship and coordinate transformation, the  $xoy$  point in the relative coordinate system can be transformed into the absolute coordinate system  $XOY$ , and the absolute coordinate of the cam profile can be expressed in matrix form as follows:

Relative coordinates  $\delta = [0, \delta_{R0}]$ , the absolute coordinates of cam pushing theory and working profile are respectively:

$$\begin{cases} \begin{pmatrix} X_p \\ Y_p \end{pmatrix} = \begin{pmatrix} \cos \frac{\delta_{Rn}}{2} & \sin \frac{\delta_{Rn}}{2} \\ -\sin \frac{\delta_{Rn}}{2} & \cos \frac{\delta_{Rn}}{2} \end{pmatrix} \begin{pmatrix} x \\ y \end{pmatrix} \\ \begin{pmatrix} X'_p \\ Y'_p \end{pmatrix} = \begin{pmatrix} \cos \frac{\delta_{Rn}}{2} & \sin \frac{\delta_{Rn}}{2} \\ -\sin \frac{\delta_{Rn}}{2} & \cos \frac{\delta_{Rn}}{2} \end{pmatrix} \begin{pmatrix} x' \\ y' \end{pmatrix} \end{cases} \quad (4)$$

Relative coordinates  $\delta = [0, \delta_{R0}]$ , the absolute coordinates of cam return theory and working profile are as follows:

$$\begin{cases} \begin{pmatrix} X_r \\ Y_r \end{pmatrix} = \begin{pmatrix} -10 \\ 01 \end{pmatrix} \begin{pmatrix} X_p \\ Y_p \end{pmatrix} = \begin{pmatrix} -\cos \frac{\delta_{Rn}}{2} & -\sin \frac{\delta_{Rn}}{2} \\ -\sin \frac{\delta_{Rn}}{2} & \cos \frac{\delta_{Rn}}{2} \end{pmatrix} \begin{pmatrix} x \\ y \end{pmatrix} \\ \begin{pmatrix} X'_r \\ Y'_r \end{pmatrix} = \begin{pmatrix} -10 \\ 01 \end{pmatrix} \begin{pmatrix} X'_p \\ Y'_p \end{pmatrix} = \begin{pmatrix} -\cos \frac{\delta_{Rn}}{2} & -\sin \frac{\delta_{Rn}}{2} \\ -\sin \frac{\delta_{Rn}}{2} & \cos \frac{\delta_{Rn}}{2} \end{pmatrix} \begin{pmatrix} x' \\ y' \end{pmatrix} \end{cases} \quad (5)$$

Relative coordinates  $\delta = [0, \delta_{Rn}]$ , the absolute coordinates of the circular arc theory and the working profile in the inner dwell stage of the cam are as follows:

$$\begin{cases} \begin{pmatrix} X_{Rn} \\ Y_{Rn} \end{pmatrix} = \begin{pmatrix} \cos \frac{\delta_{Rn}}{2} & -\sin \frac{\delta_{Rn}}{2} \\ \sin \frac{\delta_{Rn}}{2} & \cos \frac{\delta_{Rn}}{2} \end{pmatrix} \begin{pmatrix} r_0 \sin \delta \\ r_0 \cos \delta \end{pmatrix} \\ \begin{pmatrix} X'_{Rn} \\ Y'_{Rn} \end{pmatrix} = \begin{pmatrix} \cos \frac{\delta_{Rn}}{2} & -\sin \frac{\delta_{Rn}}{2} \\ \sin \frac{\delta_{Rn}}{2} & \cos \frac{\delta_{Rn}}{2} \end{pmatrix} \begin{pmatrix} (r_0 \mp r_r) \sin \delta \\ (r_0 \mp r_r) \cos \delta \end{pmatrix} \end{cases} \quad (6)$$

Relative coordinates  $\delta = [0, \delta_{Rf}]$ , the absolute coordinates of the circular arc theory and the working profile in the outer

dwell stage of the cam are respectively:

$$\begin{cases} \begin{pmatrix} X_{Rf} \\ Y_{Rf} \end{pmatrix} = \begin{pmatrix} \cos(\pi - \frac{\delta_{Rf}}{2}) \sin(\pi - \frac{\delta_{Rf}}{2}) \\ -\sin(\pi - \frac{\delta_{Rf}}{2}) \cos(\pi - \frac{\delta_{Rf}}{2}) \end{pmatrix} \\ \begin{pmatrix} (r_0 + h) \sin \delta \\ (r_0 + h) \cos \delta \end{pmatrix} \\ \begin{pmatrix} X'_{Rf} \\ Y'_{Rf} \end{pmatrix} = \begin{pmatrix} \cos(\pi - \frac{\delta_{Rf}}{2}) \sin(\pi - \frac{\delta_{Rf}}{2}) \\ -\sin(\pi - \frac{\delta_{Rf}}{2}) \cos(\pi - \frac{\delta_{Rf}}{2}) \end{pmatrix} \\ \begin{pmatrix} (r_0 + h \mp r_r) \sin \delta \\ (r_0 + h \mp r_r) \cos \delta \end{pmatrix} \end{cases} \quad (7)$$

It is convenient to get the theory and working profile of the cam by programming (1) to (7), which is convenient for manufacturing. From the above analysis and Fig. 6, it can be seen that the lift stroke (rise segment) of the cam mechanism mainly depends on the difference between the maximum radius and the minimum radius. The larger the difference, the greater the stroke of the push rod. The dwell of the push road mainly depends on  $\delta_{Rn}$  and  $\delta_{Rf}$ , and the larger  $\delta_{Rn}$  and  $\delta_{Rf}$ , the longer the dwell time.

### C. CURVATURE RADIUS OF CAM PROFILE

In order to avoid the movement distortion of the push rod, the radius of curvature of the theoretical profile should not be less than the radius of the roller, so as to avoid the sharp point of the convex profile and increase the wear. According to advanced mathematics, the theoretical profile curvature radius is calculated as follows:

$$\rho = \frac{(\dot{x}^2 + \dot{y}^2)^{\frac{3}{2}}}{\dot{x}\ddot{y} - \dot{y}\ddot{x}} > r_r \quad (8)$$

The first derivative and the second derivative of  $x$  and  $y$  is as follows:

$$\begin{cases} \dot{x} = \frac{dx}{d\delta} = \frac{ds}{d\delta} \sin \delta + (r_0 + s) \cos \delta \\ \dot{y} = \frac{dy}{d\delta} = \frac{ds}{d\delta} \cos \delta - (r_0 + s) \sin \delta \end{cases} \quad (9)$$

$$\begin{cases} \ddot{x} = \frac{d^2x}{d\delta^2} = \frac{d^2s}{d\delta^2} \sin \delta + 2 \frac{ds}{d\delta} \cos \delta - (r_0 + s) \sin \delta \\ \ddot{y} = \frac{d^2y}{d\delta^2} = \frac{d^2s}{d\delta^2} \cos \delta - 2 \frac{ds}{d\delta} \sin \delta - (r_0 + s) \cos \delta \end{cases} \quad (10)$$

Substituting (2) into (9) (10), then substituting (9) (10) into (8), the radius of curvature of the theoretical profile can be obtained. It can be seen that the radius of curvature of the theoretical profile of the cam depends on  $r_0$ ,  $h$  and  $\delta_0$ .

### D. TELESCOPIC MOTION PARAMETERS

The displacement, velocity, and acceleration of the robot during the pushing stage along the axial direction of the pipeline

are as follows:

$$\begin{cases} s_A = \frac{h_A}{2} [1 - \cos \frac{\pi}{\delta_{A0}} \delta_A] \\ \frac{ds_A}{dt} = \frac{\omega \pi h_A}{2 \delta_{A0}} \sin(\frac{\pi}{\delta_{A0}} \delta_A) \\ \frac{d^2s_A}{dt^2} = \frac{\omega^2 \pi^2 h_A}{2 \delta_{A0}^2} \cos(\frac{\pi}{\delta_{A0}} \delta_A) \end{cases} \quad (11)$$

where  $s_A$  is the displacement of the axial push rod,  $h_A$  is the stroke of the axial push rod,  $\delta_A$  is the axial cam angle,  $\delta_{A0}$  is the axial cam angle for actuating travel.

Furthermore, the relationship between CCR average step velocity and cam velocity  $n_C$ (rpm) is obtained:

$$v_{CCR} = h_A n \quad (12)$$

where  $n$  is the rotation speed of the axial cam.

Equation (12) shows that the average step velocity of CCR inchworm in-pipe robot is only related to the cam velocity and the cam rise segment. At a certain velocity, increasing the rise segment can increase the robot walking velocity.

### IV. CONSTRAINT ANALYSIS OF EXTERNAL DIMENSIONS

Pipes are divided into straight pipes and non-straight pipes according to different curvature radius. Elbow is a curved space, and the robot's contour is irregular convex geometry, so the interference analysis is very complex. In order to make the interference analysis accurate and effective, it is necessary to build a more reasonable envelope model of the robot and obtain the geometric relationship that the robot design should meet. The size of the elbow is determined by the diameter and turning radius of the elbow. The inner surface of the elbow is a space curved surface formed by scanning a circle along an arc curve. The elbow can be used to connect two vertical straight pipes. The larger the radius of curvature of the elbow is, the easier it is for the robot to pass through.

Due to the multi-point contact between the robot and the pipe wall, the outer contour of the walking robot is irregular, so it is very complex to directly analyze the interference. In this paper, multi-level cylinder geometry is used to cover the robot, and the cylinder geometry should completely cover the minimum volume (including the support legs) after the active and passive contraction of the robot. In addition, the envelope models of the first, second and  $n$ th-order combined cylindrical robots are analyzed. The envelope capability and space utilization of various models are compared and analyzed on the premise of satisfying the coverage, so as to determine the constraint relationship of the length diameter ratio under different models.

As shown in Fig. 7,  $L_p$  is defined as the pipe length dimension,  $D_p$  is the pipe diameter dimension,  $R_p$  is the pipe radius dimension,  $R_{pt}$  is the pipe turning radius,  $d_{e1}$  is the 1-order envelope cylinder diameter of robot,  $l_{e1}$  is the 1-order envelope cylinder length of robot.

From the geometric relationship in Fig. 7(a):

$$d_{e1} \leq AM \quad (13)$$

$$AM = AO - MO \quad (14)$$

$$AO = \sqrt{OB_2^2 - AB_2^2} = \sqrt{OB_1^2 - AB_1^2} \quad (15)$$

$$\begin{cases} OB_2 = R_{pt} + R_p \\ OB_1 \geq R_{pt} + R_p \\ OM = R_{pt} - R_p \end{cases} \quad (16)$$

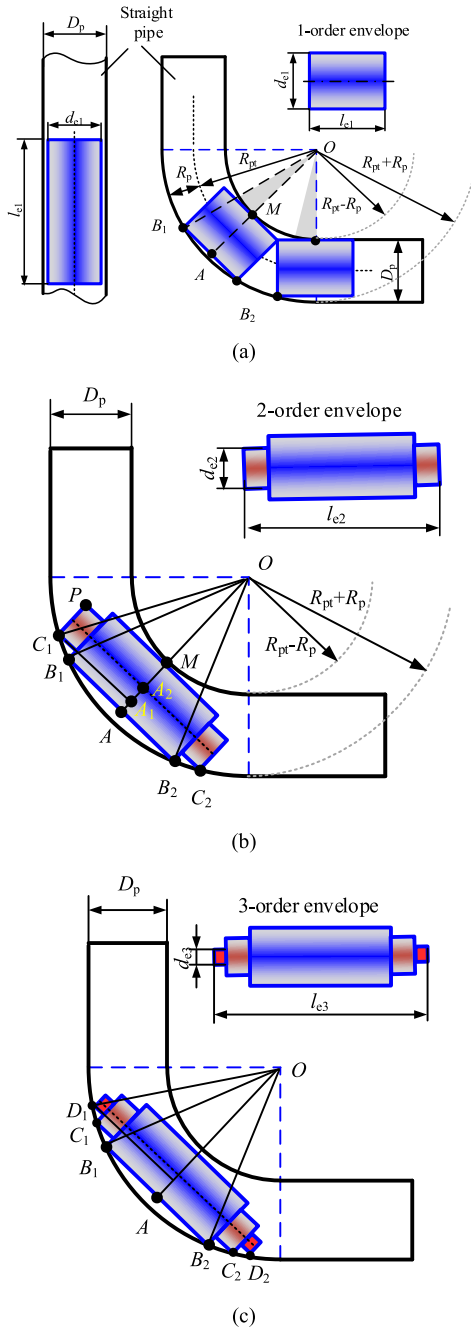


FIGURE 7. Envelope model of n-order symmetric cylinder of robot. (a) 1-order. (b) 2-order. (c) 3-order.

From (13)-(16):

$$d_{e1} \leq \sqrt{(R_{pt} + R_p)^2 - AB_2^2} - (R_{pt} - R_p) \quad (17)$$

$$AB_2 \leq \sqrt{(2R_{pt} + d_{e1})(2R_p - d_{e1})} \quad (18)$$

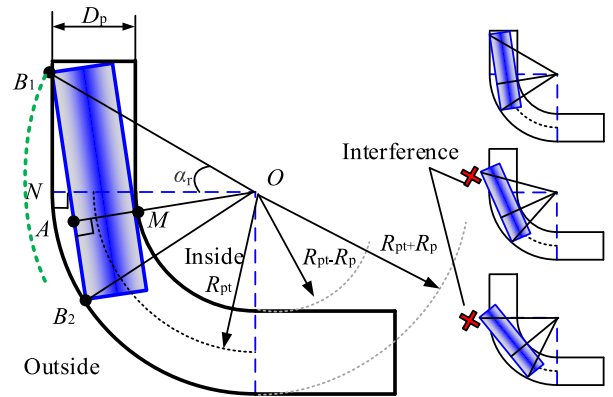


FIGURE 8. Straight-elbow pipe motion dimensional constraints.

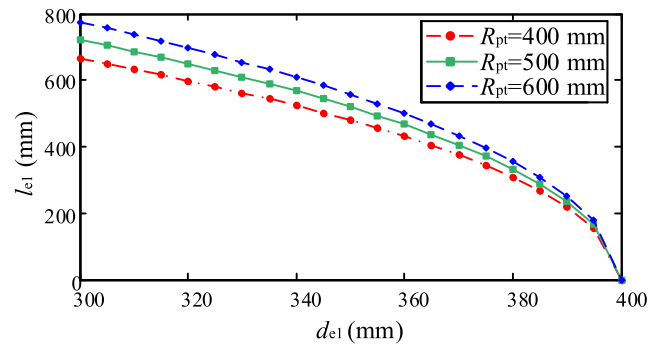


FIGURE 9. Constraint relationship of length diameter ratio under symmetric 1-order cylinder model.

$$AB_1 = AB_2 \quad (19)$$

$$l_{e1} = AB_1 + AB_2 \leq 2\sqrt{(2R_{pt} + d_{e1})(2R_p - d_{e1})} \quad (20)$$

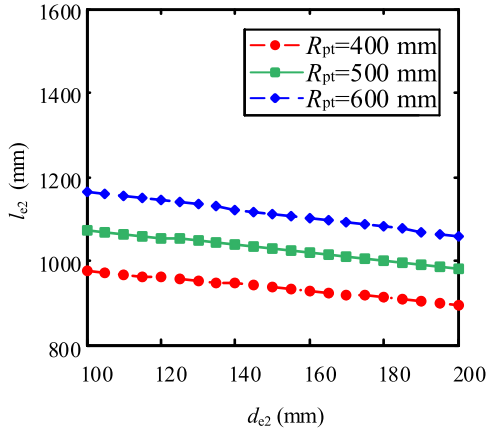
As shown in Fig. 16 and Fig. 9, the maximum allowable length of the robot mainly changes with the robot diameter. It can be found that the radius of the robot envelope cylinder decreases with the increase of the length, and the decreasing trend is faster and faster. In addition, the larger the turning radius, the longer the allowable envelope cylinder length, and the larger the available space of the robot. From Fig. 8, further analysis shows the relationship between the length and the maximum turning angle of the robot:

$$\beta_R = \frac{\pi}{2} - \alpha_r = \frac{\pi}{2} - \cos^{-1} \frac{ON}{OB_1} \quad (21)$$

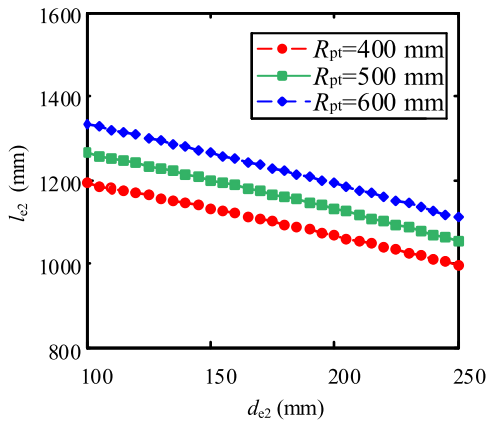
From Fig. 10, the diameter of the second-order cylinder does not exceed the diameter of the 1-order cylinder, and with the increase of the diameter of the 2-order cylinder, the limit length of the 2-order cylinder is also shrinking; in addition, the larger the diameter of the 1-order cylinder, the larger the length of the 2-order cylinder is allowed. From (21) and (22):

$$\begin{cases} ON = R_{pt} + R_p \\ OB_1^2 = AO^2 + AB_1^2 \\ AO = AM + MO = d_{e1} + R_{pt} - R_p \\ AB_1 = l_{e1} - AB_2 = l_{e1} - \sqrt{(2R_{pt} + d_{e1})(2R_p - d_{e1})} \end{cases} \quad (22)$$

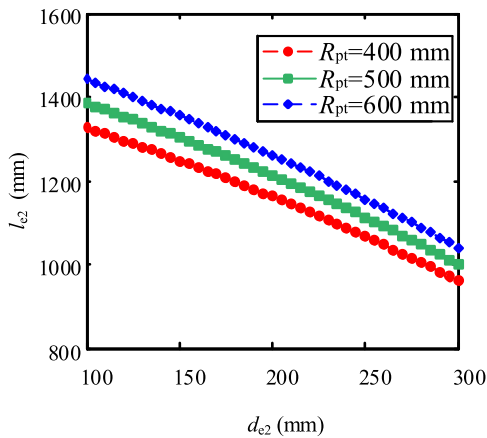
$$\beta_R = \frac{\pi}{2} - \cos^{-1} \frac{R_{pt} + R_p}{\sqrt{l_{e1}^2 + (R_{pt} + R_p)^2 - 2l_{e1}\sqrt{(2R_{pt} + d)(2R_p - d_{e1})}}} \quad (23)$$



(a)



(b)



(c)

**FIGURE 10.** Constraint relationship of length diameter ratio under Symmetric 2-order cylinder model. (a)  $d_{e1} = 200$ . (b)  $d_{e1} = 300$ . (c)  $d_{e1} = 400$ .

According to the geometric relationship, the symmetric 2-order cylindrical envelope model satisfies the following

constraints:

$$d_{e2} \leq 2A_1A_2 \quad (24)$$

$$\begin{cases} A_1A_2 = A_1O - A_2O \\ A_1O = \sqrt{(R_{pt} + R_p)^2 - (\frac{l_{e2}}{2})^2} \\ A_2O = R_{pt} - R_p + \frac{d_{e1}}{2} \end{cases} \quad (25)$$

$$d_{e2} \leq 2 \left( \sqrt{(R_{pt} + R_p)^2 - (\frac{l_{e2}}{2})^2} - (R_{pt} - R_p + \frac{d_{e1}}{2}) \right) \quad (26)$$

$$l_{e2} \leq 2\sqrt{(2R_{pt} + \frac{d_{e1} + d_{e2}}{2})(2R_p - \frac{d_{e1} + d_{e2}}{2})} \quad (27)$$

The calculation process of the envelope model of the symmetric 3-order cylinder is exactly the same as that of the symmetric 2-order cylinder. When the number of steps of the cylinder is more, the cumulative design space utilization of the robot is also higher.

$$l_{e3} \leq 2\sqrt{(2R_{pt} + \frac{d_{e1} + d_{e3}}{2})(2R_p - \frac{d_{e1} + d_{e3}}{2})} \quad (28)$$

In order to obtain the equipment volume ratio of the front and rear end area of the robot in the symmetrical 2-order cylindrical envelope model, the calculation formula of the end volume lifting ratio of the symmetrical 2-order cylindrical envelope model is:

$$\begin{aligned} V_Z &= \frac{V_{e2} - V_{e1}}{V_{e1}} = \frac{\pi d_{e2}^2(l_{e2} - l_{e1})}{\pi d_{e1}^2 l_{e1}} \\ &= \frac{d_{e2}^2(2\sqrt{(2R_{pt} + \frac{d_{e1} + d_{e2}}{2})(2R_p - \frac{d_{e1} + d_{e2}}{2})} - l_{e1})}{d_{e1}^2 l_{e1}} \end{aligned} \quad (29)$$

where  $V_Z$  is the volume lifting ratio,  $V_{ei}$  is the volume sum of the envelope cylinder of the previous  $i$  order.

Fig. 11 (a) and Fig. 11 (b) show that with the increase of the diameter of the outer cylinder of the symmetric 2-order cylinder model, the volume lifting rate increases gradually; Fig. 11 (c) shows that with the increase of the diameter of the outer cylinder of the symmetric 2-order cylinder model, the volume lifting rate increases first and then decreases, which shows that the diameter of the outer cylinder is not the bigger the better, but there is a critical value, which passes through MATLAB extremum function is easy to get.

According to the same idea above, the volume lifting rate of  $n$ -order envelope model can be deduced as follows:

From the geometric relationship:

$$\begin{cases} d_{e1} > d_{e2} \\ R_{pt} > R_p \end{cases} \quad (30)$$

$$\begin{aligned} &(2R_{pt} + \frac{d_{e2} + d_{e1}}{2})(2R_p - \frac{d_{e2} + d_{e1}}{2}) \\ &\quad - (2R_{pt} + d_{e1})(2R_p - d_{e1}) \\ &= (R_{pt} - R_p)(d_{e1} - d_{e2}) + \frac{1}{4}(d_{e2} + 3d_{e1})(d_{e1} - d_{e2}) > 0 \end{aligned} \quad (31)$$

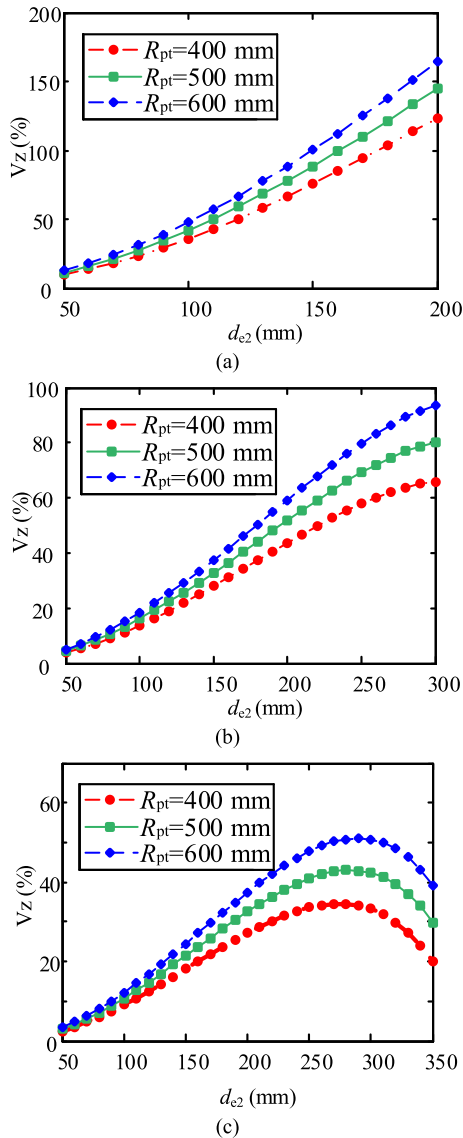


**FIGURE 11.** Relationship between volume lifting rate and diameter  $d_{e2}$  of symmetric 2-order cylinder model outer cylinder. (a)  $d_{e1} = 200$ . (b)  $d_{e1} = 300$ . (c)  $d_{e1} = 350$ .

From (31):

$$2\sqrt{(2R_{pt} + \frac{d_{e2} + d_{e1}}{2})(2R_p - \frac{d_{e2} + d_{e1}}{2})} > 2\sqrt{(2R_{pt} + d_{e1})(2R_p - d_{e1})} \quad (32)$$

Therefore, by using the symmetrical 2-order cylinder simplified model, the axial dimension of the robot can be expanded, and the design space utilization rate can be improved, which is convenient for the rigid loading of large and medium-sized cameras and other equipment.

### V. ANALYSIS OF MECHANICAL PROPERTIES

The tractive ability of in-pipe robot mainly depends on its own axial thrust and maximum static friction, which is the product of positive contact pressure and friction coefficient of pipeline wall. When the contact positive pressure of the motor power

and friction coefficient of the robot is greater and the traction force generated by the robot is greater, the following analysis is carried out.

#### A. DYNAMIC PUSHING FORCE ANALYSIS

The static balance force analysis process of axial and radial cams is similar, without considering the friction and gravity of the motion pair. The static balance force equation of the simplified mechanical model is shown in (38):

(1)Static balance force analysis

$$F_P = \frac{T}{2 \frac{ds}{d\delta}} = \frac{\delta_{A0}T}{\pi h \sin(\frac{\pi}{\delta_{A0}} \delta_A)} \quad (33)$$

where  $F_P$  is the pushing force of the cam mechanism along the axial direction of the pipeline.  $T$  is the axial cam torque,  $\delta_A$  is axial cam angle,  $\delta_{A0}$  is axial cam angle for actuating travel.

Assuming that the rear body RB of the robot is locked against the pipe wall, and the front body moves along the axial direction of the pipeline as a whole, it can be simplified as a mass block. Therefore, dynamic force analysis introduces the inertia force of the front body FB on the basis of static force analysis. The dynamic force analysis is as follows.

(2)Dynamic balance force analysis

$$F_P = \frac{\delta_{A0}T}{\pi h_A \sin(\frac{\pi}{\delta_{A0}} \delta_A)} - F_I \quad (34)$$

$$F_I = m_F \frac{\omega^2 \pi^2 h_A}{2\delta_{A0}^2} \cos(\frac{\pi}{\delta_{A0}} \delta_A) \quad (35)$$

where  $F_I$  is the equivalent inertia force of the front body,  $h_A$  is the stroke of the axial push rod,  $m_F$  is the mass of the front body.

Substituting equation (35) into equation (34):

$$F_P = \frac{\delta_{A0}T}{\pi h_A \sin(\frac{\pi}{\delta_{A0}} \delta_A)} - m_F \frac{\omega^2 \pi^2 h_A}{2\delta_{A0}^2} \cos(\frac{\pi}{\delta_{A0}} \delta_A) \quad (36)$$

From (36), it can be seen that the dynamic inertia force is not only related to the cam angular velocity, cam angle for actuating travel, and actuating travel, but also to the mass and acceleration of the front body of the CCR, so the lightweight of the robot is beneficial for improving the dynamic performance of the robot.

The radial telescopic mechanism has a lightweight push rod and low cam speed, and the steady-state force balance analysis can meet the application needs. However, for axial telescopic motion, the mass and inertia force of the robot's front and rear body are much larger than those of the radial support legs. Therefore, using ADAMS to analyze the influence of inertia force on the reaction force of the vehicle cam bearing provides a reference basis for obtaining the maximum critical speed of the robot cam. In order to adapt to the low-speed working conditions of pipeline inspection and operation and improve the load capacity, the actual speed of the cam after deceleration does not exceed 120 r/min, while less than 60 r/min leads to low walking efficiency. Therefore, the



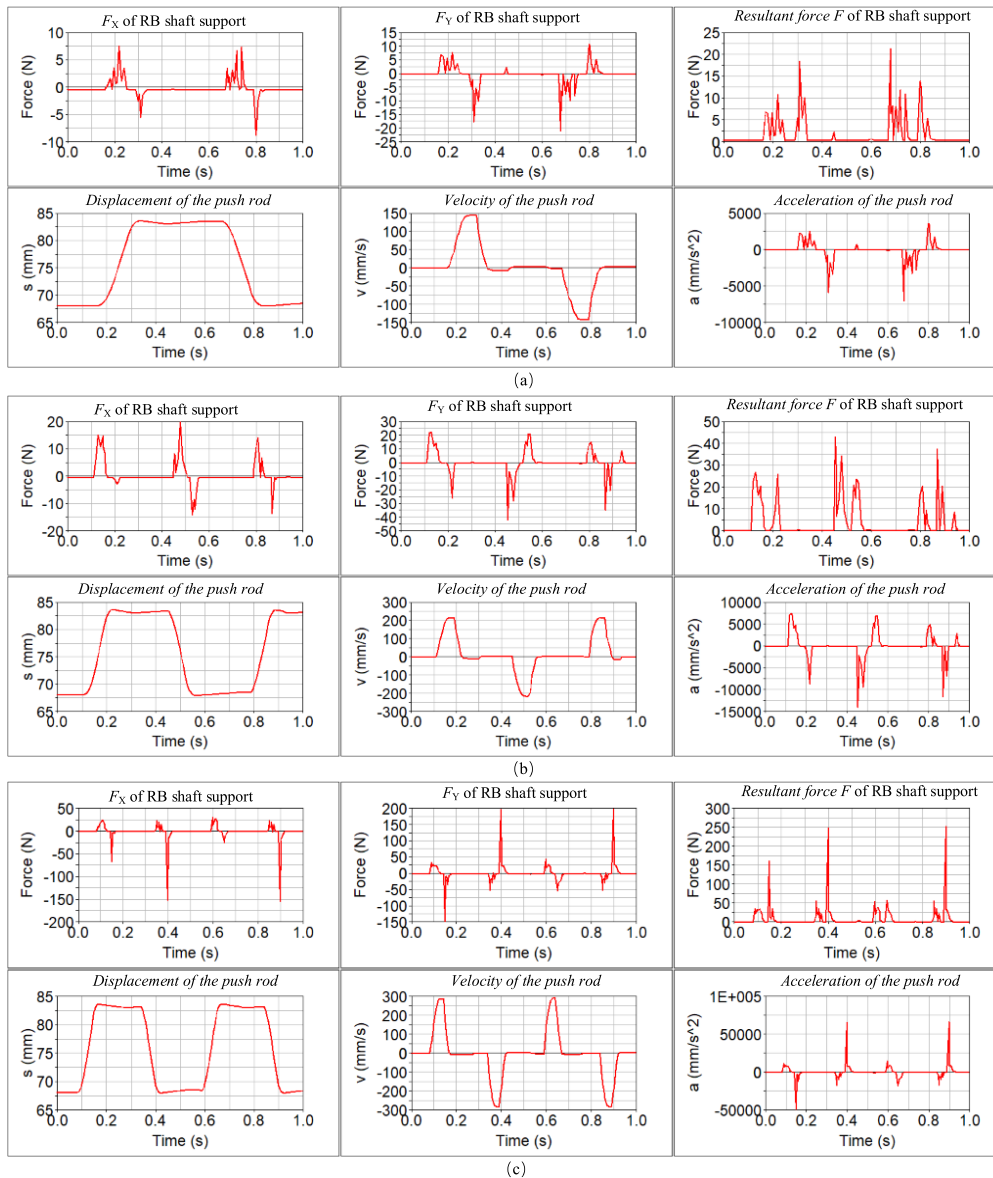


**FIGURE 12.** Adams dynamic simulation analysis. (a) Cam rotation speed 60r/min. (b) Cam rotation speed 90r/min. (c) Cam rotation speed 120r/min.

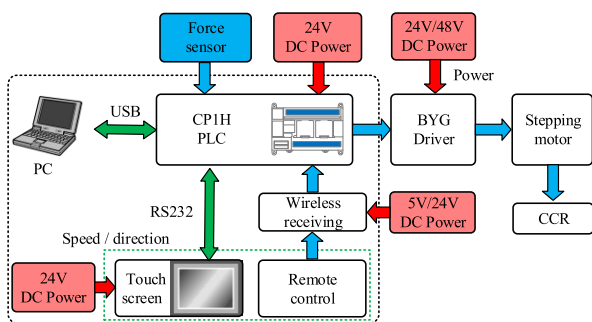


**FIGURE 13.** Test system schematic diagram of CCR.

cam simulation speeds were selected as 60 r/min, 90 r/min, and 120 r/min for simulation.

The simulation results are shown in Fig. 12. When the cam speed is 60r/min and 90r/min, the reaction force of the

camshaft support along the pipeline axis is very small, not exceeding 30N. When the cam speed is 120r/min, the reaction force of the camshaft seat along the pipeline axis rapidly increases to 200N, which is not conducive to stable locking of the body. Therefore, the critical speed of the cam should be controlled at 90 r/min.

### B. TRACTION ENERGY EFFICIENCY RATIOS

The traction energy efficiency ratios of single-drive and three drives robots are respectively

$$FPR_1 = \frac{F_P \eta_G}{P} \quad (37)$$

$$FPR_3 = \frac{F_P}{3P} \quad (38)$$

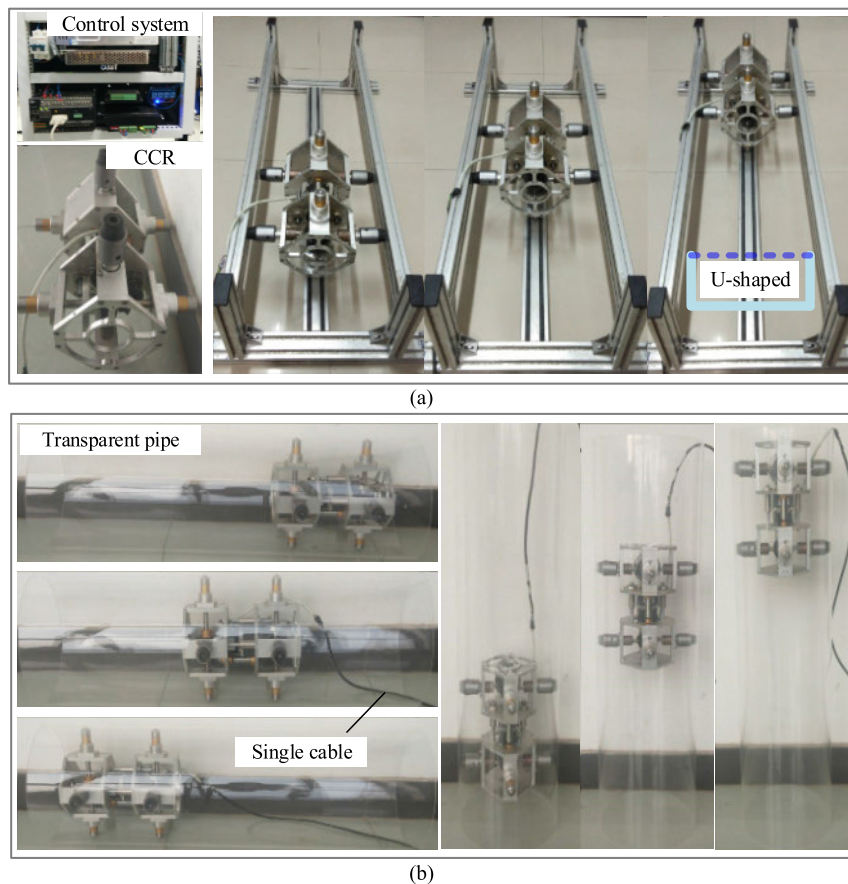


**FIGURE 14.** Principle verification of CCR in the transparent pipe. (a) Testing within a rectangular frame. (b) Testing inside a transparent circular pipe.

where  $P$  is the motor power,  $\eta_G$  is the mechanical transmission efficiency of the two-stage gears (cylindrical and bevel gears).

Equation (37) divided by equation (38):

$$\frac{FPR_1}{FPR_3} = 3\eta_G \approx 2.7 \quad (39)$$

The CCR adopts a two-stage transmission of spur and bevel gears, both of which are open gear transmission with good running-in and thin oil lubrication. According to the transmission efficiency table of mechanisms [33], the transmission efficiency of the spur and bevel gears is generally 0.95. Equation (39) shows that the traction energy efficiency ratio is more than 2 times of the original. This shows that the single-drive inchworm in-pipe robot can greatly improve the traction energy efficiency ratio, which has obvious application advantages in the pipeline environment.

## VI. PRINCIPLE VERIFICATION

As illustrated in Fig. 13, the hardware of the control system mainly includes: switch power supply, CPH-PLC, touch screen, remote control, and motor driver. The start, stop, forward and backward movement of the robot in the pipe can be controlled by a touch screen or remote control. The BYG

driver is used to drive the step motor. The supply voltage of the BYG is 48V, and the supply voltage of the touch screen is 24V. RS232 communication is used between the touch screen and CPH.

As shown in Fig. 14 (a), the robot walking tests inside an aluminum profile frame, which resembles a U-shaped or rectangular interface. Due to the robot's total of 8 supporting legs and wheels, its front or rear body can support up to four points (up, down, left, and right), making it compatible with three-point support scenarios (bottom, left, and right). As shown in Fig. 14(b), the robot was tested in both horizontal and vertical transparent tubes, by observing the transparent tube, it can be observed that the robot is only dragging a cable rope, which is because the robot only uses one motor and one driver. Therefore, the control complexity and number of cables of the robot have been reduced. If the motor rotates forward, the robot will walk forward; if the motor rotates backwards, the robot will walk backwards. The robot can achieve bidirectional movement in both horizontal and vertical directions. The experimental results show that the bidirectional gait movement of the robot can be realized by controlling only one motor, and the multi drive control of the inchworm in-pipe robot is greatly simplified.

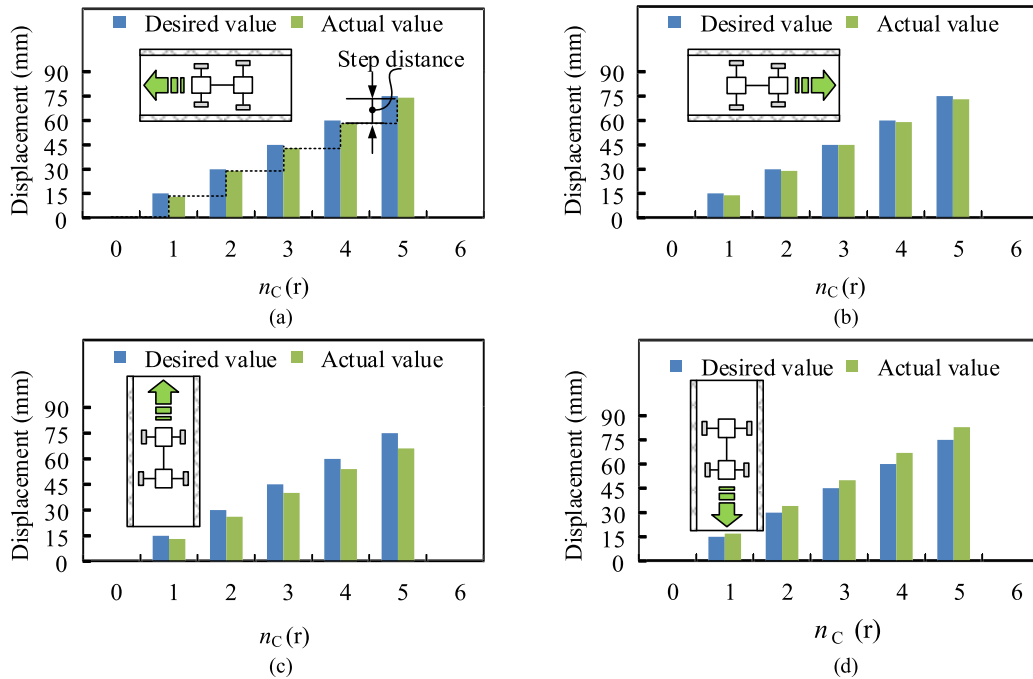


**FIGURE 15.** The relationship between displacement of gait motion and the number of cam rotations. (a) Move left. (b) Move right. (c) Move up. (d) Move down.

Compared with several other robots in Table 1, CCR could get a two-way creeping walk via only one driver, thus the control is simple. In addition, CCR adopts an active support method to avoid sliding friction between the support legs and the pipe wall. For the inchworm in-pipe robot, the most important thing is that the number of motors is reduced, so that the number of motor power lines is reduced to 1/3 of the original, so the drag of streamer is greatly reduced.

**TABLE 1.** Comparison with other inchworm in-pipe robots.

N.O.	1[30]	2[32]	3 CCR
Type	Inchworm	Inchworm	Inchworm
Adhesion method	Passive	Active	Active
Number of drives	1	3	1
Control difficulty	Simple	Medium	Simple
Walking direction	One-way	Two-way	Two-way
Driving actuator	1 cylinder	3 motors	1 motor

In addition, displacement tests were conducted on the robot to obtain the relationship between the number of cam rotations and displacement. The theoretical displacement satisfies the following equation:

$$s = h_A n_C \tag{40}$$

where  $s$  is the theoretical displacement of the robot CCR,  $n_C$  is the number of revolutions of the axial cam.

The displacement test results in Fig. 15 show that the average displacement errors for horizontal and vertical walking are 2.0% and 11.3%, respectively. Vertical walking has a relatively large error compared to horizontal walking, which is caused by the deformation of the robot’s telescopic legs under the action of gravity. Due to the cantilever structure of the telescopic leg, the longer the length of the leg, the greater the error. Therefore, the telescopic leg should not be too long and should be designed and adapted to the diameter of the pipe. To reduce the error, it is possible to reduce the weight of the robot or increase the stiffness of the support legs in the future. Equation (40) is only used as a theoretical displacement calculation method for robots, and errors should be taken into account when estimating the actual displacement. In addition, the displacement information of the robot can be better obtained by combining it with other advanced positioning systems.

## VII. CONCLUSION

In this paper, a single-motor driven inchworm in-pipe robot, called CCR, has been designed. CCR, which is based on a cam combination mechanism, can realize crawling and active supporting motion with only one motor, which avoids the sequential or coordinated control between multiple drives and greatly simplifies the control factors. With the reduction of the number of drives, it is easier to improve safety in pipelines containing flammable and explosive gases.

Through the mechanism design and parameter analysis of the proposed robot, the kinematic law was obtained. Through the analysis of the constraint characteristics in the pipe,

the constraint relationship of the length-diameter ratio was determined to avoid the interference in the pipe. The n-order symmetric cylinder envelope model was used, which greatly improves the robot volume ratio and the space utilization rate in the pipe. The dynamic characteristics of the robot were obtained by simulation using ADAMS software. Finally, the effectiveness of the robot's bi-directional movement in horizontal and vertical pipelines was verified through experiments.

Future work could include a rigorous study of the effects of other parametric changes and different loading conditions, as well as the study of pipes of different shapes and materials.

## REFERENCES

- [1] J. T. Kahnemouei and M. Moallem, "A comprehensive review of in-pipe robots," *Ocean Eng.*, vol. 277, Jun. 2023, Art. no. 114260.
- [2] A. Verma, A. Kaiwart, N. D. Dubey, F. Naseer, and S. Pradhan, "A review on various types of in-pipe inspection robot," *Mater. Today, Proc.*, vol. 50, pp. 1425–1434, Sep. 2022.
- [3] A. Kakogawa, K. Murata, and S. Ma, "Automatic T-branch travel of an articulated wheeled in-pipe inspection robot using joint angle response to environmental changes," *IEEE Trans. Ind. Electron.*, vol. 70, no. 7, pp. 7041–7050, Jul. 2023.
- [4] Z. Wu, Y. Wu, S. He, and X. Xiao, "Hierarchical fuzzy control based on spatial posture for a support-tracked type in-pipe robot," *Trans. Can. Soc. Mech. Eng.*, vol. 44, no. 1, pp. 133–147, Mar. 2020.
- [5] Q. Xie, S. Liu, and X. Ma, "Design of a novel inchworm in-pipe robot based on cam-linkage mechanism," *Adv. Mech. Eng.*, vol. 13, no. 9, Sep. 2021, Art. no. 16878140211045193.
- [6] B. Jang, J. Nam, W. Lee, and G. Jang, "A crawling magnetic robot actuated and steered via oscillatory rotating external magnetic fields in tubular environments," *IEEE/ASME Trans. Mechatronics*, vol. 22, no. 3, pp. 1465–1472, Jun. 2017.
- [7] J. Kim, H. Kim, Y. Kim, J. Park, T. Seo, H. S. Kim, and J. Kim, "A new lizard-inspired robot with S-shaped lateral body motions," *IEEE/ASME Trans. Mechatronics*, vol. 25, no. 1, pp. 130–141, Feb. 2020.
- [8] H. Torajizadeh, A. Asadirad, E. Mashayekhi, and G. Dabiri, "Design and manufacturing a novel screw-in-pipe inspection robot with steering capability," *J. Field Robot.*, vol. 40, no. 3, pp. 429–446, May 2023.
- [9] Y. Zhong, Z. Li, and R. Du, "A novel robot fish with wire-driven active body and compliant tail," *IEEE/ASME Trans. Mechatronics*, vol. 22, no. 4, pp. 1633–1643, Aug. 2017.
- [10] S. Wang, Y. Wang, Q. Wei, M. Tan, and J. Yu, "A bio-inspired robot with undulatory fins and its control methods," *IEEE/ASME Trans. Mechatronics*, vol. 22, no. 1, pp. 206–216, Feb. 2017.
- [11] K. Thung-Od, K. Kanjanawanishkul, T. Maneewarn, T. Sethaput, and A. Boonyaprasorn, "An in-pipe inspection robot with permanent magnets and omnidirectional wheels: Design and implementation," *Appl. Sci.*, vol. 12, no. 3, p. 1226, Jan. 2022.
- [12] X. Miao, H. Zhao, F. Song, and Y. Ma, "Dynamic characteristics and motion control of pipeline robot under deformation excitation in subsea pipeline," *Ocean Eng.*, vol. 266, Dec. 2022, Art. no. 112790.
- [13] H. Sawabe, M. Nakajima, M. Tanaka, K. Tanaka, and F. Matsuno, "Control of an articulated wheeled mobile robot in pipes," *Adv. Robot.*, vol. 33, no. 20, pp. 1072–1086, Oct. 2019.
- [14] Y. Zhang and G. Yan, "In-pipe inspection robot with active pipe-diameter adaptability and automatic tractive force adjusting," *Mechanism Mach. Theory*, vol. 42, no. 12, pp. 1618–1631, Dec. 2007.
- [15] F. Munoz, G. Alici, H. Zhou, W. Li, and M. Sitti, "Analysis of magnetic interaction in remotely controlled magnetic devices and its application to a capsule robot for drug delivery," *IEEE/ASME Trans. Mechatronics*, vol. 23, no. 1, pp. 298–310, Feb. 2018.
- [16] D. Shiomi and T. Takayama, "Tapered, twisted bundled-tube locomotive devices for stepped pipe inspection," *Sensors*, vol. 22, no. 13, p. 4997, Jul. 2022.
- [17] J. Nam, W. Lee, J. Kim, and G. Jang, "Magnetic helical robot for targeted drug-delivery in tubular environments," *IEEE/ASME Trans. Mechatronics*, vol. 22, no. 6, pp. 2461–2468, Dec. 2017.
- [18] T. Li, "Design and motion mechanism of a screw drive in-pipe robot with adaptability to in-pipe environment," *J. Mech. Eng.*, vol. 52, no. 9, pp. 9–17, 2016.
- [19] T. Ren, Y. Zhang, Y. Li, Y. Chen, and Q. Liu, "Driving mechanisms, motion, and mechanics of screw drive in-pipe robots: A review," *Appl. Sci.*, vol. 9, no. 12, p. 2514, Jun. 2019.
- [20] R. Tao, Y. Chen, and L. Qingyou, "A helical drive in-pipe robot based on compound planetary gearing," *Adv. Robot.*, vol. 28, no. 17, pp. 1165–1175, Sep. 2014.
- [21] R. Tao, L. Qingyou, L. Yujia, and C. Yonghua, "Basic characteristics of a novel in-pipe helical drive robot," *Int. J. Mechatronics Autom.*, vol. 4, no. 2, pp. 127–136, 2014.
- [22] Y. Chen, Q. Liu, and T. Ren, "A simple and novel helical drive in-pipe robot," *Robotica*, vol. 33, no. 4, pp. 920–932, Mar. 2014.
- [23] Y. Li, Q. Liu, and W. Li, "Development of a novel oil and gas in-pipe robot," *Int. J. Mechatron. Manuf. Syst.*, vol. 8, no. 3, pp. 102–115, Jan. 2015.
- [24] D. Fang, G. Jia, J. Wu, X. Niu, P. Li, R. Wang, Y. Zhang, and J. Zhang, "A novel worm-like in-pipe robot with the rigid and soft structure," *J. Bionic Eng.*, vol. 13, pp. 1–11, Jun. 2023, doi: 10.1007/s42235-023-00395-1.
- [25] F. Ito, I. Horiuchi, K. Tsuru, and T. Nakamura, "Development of an earthworm-type electrical wire installation assistance robot using artificial muscles," *IEEE Robot. Autom. Lett.*, vol. 8, no. 5, pp. 2999–3006, May 2023.
- [26] Y. Liu, X. Dai, Z. Wang, Q. Bi, R. Song, J. Zhao, and Y. Li, "A tensegrity-based inchworm-like robot for crawling in pipes with varying diameters," *IEEE Robot. Autom. Lett.*, vol. 7, no. 4, pp. 11553–11560, Oct. 2022.
- [27] X. Dai, Y. Liu, W. Wang, R. Song, Y. Li, and J. Zhao, "Design and experimental validation of a worm-like tensegrity robot for in-pipe locomotion," *J. Bionic Eng.*, vol. 20, no. 2, pp. 515–529, Mar. 2023.
- [28] C. Tang, B. Du, S. Jiang, Q. Shao, X. Dong, X.-J. Liu, and H. Zhao, "A pipeline inspection robot for navigating tubular environments in the sub-centimeter scale," *Sci. Robot.*, vol. 7, no. 66, pp. 1–13, May 2022.
- [29] J. Liu, G. Ma, Z. Ma, and S. Zuo, "Origami-inspired soft-rigid hybrid contraction actuator and its application in pipe-crawling robot," *Smart Mater. Struct.*, vol. 32, no. 6, Jun. 2023, Art. no. 065015.
- [30] J.-W. Qiao, J.-Z. Shang, X. Chen, Z.-R. Luo, and X.-P. Zhang, "Unilateral self-locking mechanism for inchworm in-pipe robot," *J. Central South Univ. Technol.*, vol. 17, no. 5, pp. 1043–1048, Oct. 2010.
- [31] D. Zarrouk and M. Shoham, "Analysis and design of one degree of freedom worm robots for locomotion on rigid and compliant terrain," *J. Mech. Des.*, vol. 134, no. 2, Feb. 2012, Art. no. 021010.
- [32] J. Yang, Y. Xue, J. Shang, and Z. Luo, "Research on a new bilateral self-locking mechanism for an inchworm micro in-pipe robot with large traction," *Int. J. Adv. Robot. Syst.*, vol. 11, no. 16, pp. 1–11, Oct. 2014.
- [33] H. Sun, Z. Chen, and W. Ge, "Mechanical efficiency and self-locking," in *Theory of Machines and Mechanisms*, 8th ed. Beijing, China: HEP, 2013, ch. 5, sec. 1, pp. 75–77.



**QIZHI XIE** received the M.S. degree in mechanical engineering from Zhejiang Sci-Tech University, Hangzhou, China, in 2016, and the Ph.D. degree in mechanical design and theory from the China University of Mining and Technology, Xuzhou, China, in 2020.

As the Project Leader, he has presided Xuzhou Key Research and Development Project, Jiangsu Province Industry University Research Cooperation Project, and participated in National Key Research and Development Program of China "Intelligent Robot." He is currently a Lecturer with the School of Mechanical and Electrical Engineering, Xuzhou University of Technology, Xuzhou. He has obtained over ten invention patent authorizations from China, USA, and Japan. He has published an article in the top journal *Mechanism and Machine Theory*. His current research interests include in-pipe robots, mechanical design, and intelligent control.



**SONG CUI** received the M.S. degree in mechanical engineering from the Anhui University of Science & Technology, Huainan, China, in 2018. He is currently pursuing the Ph.D. degree in mechanical design and theory with the China University of Mining and Technology, Xuzhou, China.

He is also a Visiting Student with the University of Alberta, Edmonton, Canada. His current research interests include mobile robots, mechanical design, and machinery dynamics.



**PEILIN CHENG** received the M.S. degree in mechanical engineering and the Ph.D. degree in mechanical design and theory from Zhejiang Sci-Tech University, Hangzhou, China, in 2018 and 2023, respectively.

He is currently an Assistant Researcher with Zhejiang Sci-Tech University, Hangzhou. He has obtained over ten invention patent authorizations. He has published over five articles in journals, such as *Robotica* and *Journal of Mechanisms and Robotics-Transactions of the ASME*. His current research interests include in-pipe robots, mechanical design, and soft robots.



**QIANG LIU** received the M.S. degree in mechanical engineering from the Wuhan University of Technology, Wuhan, China, in 2011. He is currently pursuing the Ph.D. degree with the China University of Mining and Technology.

He is also an Associate Professor with the Xuzhou University of Technology, Xuzhou, China. He has participated in the Horizontal Project of XCMG Group's "Research and Industrialization of Core Technology for Hundred Ton Electric Drive Dump Trucks" as a Technical Supervisor. His current research interests include mobile robots, construction machinery, and mining machinery.

• • •